



Local hydroxyl enhancement design of NiFe sulfide electrocatalyst toward efficient oxygen evolution reaction

Xiaojing Liu, Ximeng Zhao, Shuyi Cao, Mingyi Xu, Yanji Wang, Wei Xue ^{*}, Jingde Li ^{*}

Hebei Provincial Key Laboratory of Green Chemical Technology and High Efficient Energy Saving, National-Local Joint Engineering Laboratory for Energy Conservation of Chemical Process Integration and Resources Utilization, Tianjin Key Laboratory of Chemical Process Safety, School of Chemical Engineering and Technology, Hebei University of Technology, Tianjin 300130, China

ARTICLE INFO

Keywords:

Oxygen evolution reaction
Local OH⁻ enrichment effect
N-doped carbon nanotube
NiFe sulfide
Dynamic evolution

ABSTRACT

Herein, a local OH⁻ reactant concentration enhancement design is proposed towards efficient oxygen evolution reaction (OER) electrocatalyst. In this strategy, N-doped carbon nanotubes (NCNT), serving as conductive OH⁻ concentration enhancement matrix, are introduced near the adjacent Fe-NiS₂ catalyst to accelerate OER reaction by promoting the local mass transfer process. This OH⁻ enhancement effect is originated from the electropositive OH⁻ absorption sites of NCNT and local-electronic field induced by conductive three-dimensional NCNT network that synergistically works with adjacent Fe-NiS₂ nanocatalyst. Accordingly, the Fe-NiS₂/NCNT catalyst only requires low overpotential of 247 mV at 100 mA cm⁻², outperforms most of recently reported OER catalysts. The anion-exchange membrane water electrolyzer reaches 500 mA cm⁻² at 1.70 V_{cell}. Analysis also reveals that, this enhanced local concentration design promotes the conversion of Fe-NiS₂ into S, Fe co-doped NiOOH, which is the real OER active component. This work provides an alternative strategy to develop high-efficiency OER electrocatalysts.

1. Introduction

Oxygen evolution reaction (OER) plays an important role in alkaline water splitting reaction for hydrogen production [1,2]. However, due to the complex four-electron transfer process and slow reaction kinetics of OER process, highly efficient electrocatalysts are urgently needed to improve the energy efficiency of water splitting [3,4]. The well-known OER catalysts are noble metal-based materials, such as IrO₂ and RuO₂. However, their high cost and scarcity have severely restricted their wide applications [5]. Therefore, there is an increasing demand for low-cost and high performance OER catalysts.

The most widely reported non-precious OER catalysts are transition metal-based compounds, e.g. Ni/Fe/Co hydroxides [6,7], dichalcogenides [8,9], nitrides [10,11] and phosphides [12,13]. To achieve high OER activity, various strategies are developed including tuning the electronic state Ni/Fe/Co-species by cation/anion heteroatom-doping [14], porous high specific area structure design for increased active sites exposure [15], superhydrophilic/superaerophobic treatment of the catalyst surface to accelerate the oxygen gas release process [16], and manipulation of the catalyst oxidation state into highly active oxy-hydroxide species [17–19]. That is, most of these methods focused on

catalyst structure and surface state regulation to improve the OER performance.

Recently, the utilization of intermediate confinement effect, tip-enhanced local electric field and construction of local coordination environment to enrich the local reactant concentration in the vicinity of the catalytic sites has been found very effective to promote the CO₂ electrochemical reduction and hydrogen evolution reaction [20–22]. This local reactant concentration strategy provides an alternative way to promote the performance of electrochemical reactions. Accordingly, one can expect that, enhancing the local concentration of OH⁻ reactant around the catalyst surface can be an effective strategy for improving OER efficiency. The reactant enrichment strategy reported in the literature is achieved by the nanoporous conformation and field-effect endowed through the catalyst structure design. In other words, the enhancement of reactant concentration is resulted from the unique structure of the catalysts. This usually requires sophisticated design of nanocatalysts posing a great challenge for catalyst fabrication. Therefore, an alternative solution can be the introduction of additional reactant attractor around the catalysts. The reactant attractor should be conductive and has efficient adsorption site towards OH⁻ ions. Such design would lead to increased OH⁻ concentration around the catalyst

* Corresponding authors.

E-mail addresses: weixue@hebut.edu.cn (W. Xue), jingdeli@hebut.edu.cn (J. Li).



surface and thus promote the OER reaction. To the authors' knowledge, this reactant attractor introduction design in OER electrocatalysts has not reported in the literature.

In this work, a nitrogen-doped carbon nanotube (NCNT) facilitated local OH⁻ concentration enhancement design is proposed for the development of efficient OER catalyst. The higher electronegativity of nitrogen (3.04) over carbon (2.55) would result into positively charged carbon atoms in NCNT. The latter acts as the active sites facilitating the attraction of OH⁻ reactant. Meanwhile, NCNT provides a three-dimensional high-efficiency conductive network with interlinked electron transfer pathways. Therefore, in this strategy, NCNT-adorned carbon cloth substrate serves as three-dimensional conductive OH⁻ attractor to enhance its local concentration. Then, Fe-doped NiS₂ (Fe-NiS₂) nanosheets are introduced within the NCNT network as the catalytic active center towards OER. Benefited from the enhanced local reaction concentration design, the resulting Fe-NiS₂/NCNT electrocatalyst achieves a low overpotential of 247 mV at 100 mA cm⁻² in 1.0 M KOH. Also, the anion-exchange membrane (AEM) water electrolyzer delivers a cell current density of 500 mA cm⁻² at only 1.70 V_{cell} with long-term durability performance. Experimental analysis also shows that the enhanced local of OH⁻ species accelerate the conversion of Fe-NiS₂ into S and Fe co-doped NiOOH (S, Fe-NiOOH) species. This hydroxide species is highly active towards OER with optimized electronic and promoted reaction kinetics. This work provides a promising alternative strategy for the design of efficient OER catalysts for alkaline water electrolysis.

2. Computational and experimental section

2.1. Density function theory (DFT) calculation

The DFT calculations are conducted by the VASP package within the generalized gradient approximation (GGA) using the PBE functional. The plane-wave kinetic energy cutoff is 400 eV. The K-points mesh is set to 2 × 2 × 1. The periodic slab is separated by a vacuum height of 15 Å. The energy and force criterion for convergence are set at 10⁻⁵ eV and 0.03 eV/Å, respectively. The reaction transition states (TS) is searched using the climbing image nudged elastic band (CI-NEB) method. The Hubbard U term is corrected by DFT+U calculations introduced by Dudarev et al. with U-J parameters of 5.0 and 5.5 for Fe and Ni, respectively. The calculations are conducted using realistic catalytic phases, e.g. NiOOH, Fe-NiOOH and S, Fe-NiOOH, revealed by in-situ Raman analysis. The Fe-NiOOH model is constructed by replacing two Ni atoms in the NiOOH slab with two Fe atoms. Then, an O atom in Fe-NiOOH is replaced by an S atom to construct the S, Fe-NiOOH model.

2.2. COMSOL Multiphysics simulation

The OH⁻ concentration near the Fe-NiS₂/NCNT electrode is simulated using a two-dimensional model in COMSOL Multiphysics. The Gauss's law is used to compute charge density: $\rho = \epsilon_r \epsilon_0 \nabla \cdot E$, where ϵ_0 and ϵ_r represents the dielectric function for vacuum and electrolyte, respectively; the electric field E is computed as: $E = -\nabla V$. The electrical double layer is described using the Gouy-Chapman-Stern model considering Helmholtz and diffusion layer. The Poisson-Nerst-Planck equations are solved in steady state equilibrium between electrostatic forces and diffusion [23]:

$$\nabla^2 V = \begin{cases} 0, & d < d_H \\ (c_K - c_{OH})F, & d > d_H \end{cases}$$

where d represents the distance between electrode surface and electrolyte, and d_H is the thickness of the Helmholtz layer, which is taken as the radius of OH⁻ (0.137 nm) [24]. Therefore, $d < d_H$ represents within the Helmholtz layer, and $d > d_H$ refers to in the diffusion layer.

2.3. Synthesis of NCNT on carbon cloth substrate

First, carbon cloth is treated in a mixed acid solution of nitric acid and sulfuric acid for 12 h, and then washed with distilled water. Then, the carbon cloth sample is soaked in 10 mL Ni(NO₃)₂·6 H₂O ethanol solution (0.5 mol L⁻¹) and dried under room temperature. After that, N, N-dimethylformamide (DMF), as a carbon source, is placed in the upstream zone of the quartz tube, and the soaked carbon cloth is placed in the center of the tube furnace. When DMF vapor is introduced along with the Ar gas from the upstream and heated at 700 °C for 3 h, N-doped CNT (NCNT) is grown on carbon cloth fibers.

2.4. Synthesis of Fe-NiS₂/NCNT

The Fe-NiS₂/NCNT is developed by sulphurization treatment of NiFe layered double hydroxide (NiFe LDH/NCNT). The latter is synthesized through hydrothermal method as follows: 4 mmol Ni(NO₃)₂·6 H₂O, 1 mmol Fe(NO₃)₂·9 H₂O, 2 mmol NH₄F, and 5 mmol urea are dissolved in 35 mL deionized water. The solution is transferred to the Teflon-lined stainless-steel autoclave. Then, the NCNT sample is put into the autoclave and heated at 120 °C for 3 h. The resulting NiFe LDH/NCNT product is washed with ethanol and water. The Fe-NiS₂/NCNT sample is synthesized by sulfuration treatment of NiFe-LDH/NCNT. In the experiment, 0.5 g sulfur powder and NiFe LDH/NCNT are placed in the up and downstream zone of the tube furnace, respectively. The furnace is heated in Ar atmosphere at 300 °C for 2 h with a ramping rate of 2 °C min⁻¹. The obtained product is Fe-NiS₂/NCNT and the catalyst loading is about 1.5 mg/cm². The Fe-NiS₂ control sample is prepared through sulfuration treatment of NiFe LDH that grown directly on carbon cloth substrate using the same procedure in the NiFe LDH/NCNT preparation.

2.5. Structural characterization

X-ray diffraction (XRD) patterns are recorded on Bruker D8 FOCUS X-ray diffractometer with Cu K α (40 kV, 100 mA) radiation. The scanning electron microscope (SEM) images are obtained with a Hitachi S-4800 electron microscope. The transmission electron microscopy (TEM) and element mapping images are recorded by a JEM-2100 F field emission electron microscope at an acceleration voltage of 200 kV. *In-situ* Raman spectroscopy is recorded on the InVia Reflex instrument. Zeta potential measurements are carried out using Zetasizer Nano ZS90 device by Malvern Instruments. X-ray photoelectron spectra (XPS) is acquired on an ESCALAB 250 spectrometer to characterize the surface composition of the samples. The specific surface areas and corresponding pore size distributions are evaluated using the Brunauer-Emmett-Teller (BET) method by N₂ adsorption-desorption process isotherms with Autosorb iQ-MP-MP instrument. Contact angles are measured on a KRUSS DSA-100D apparatus with 1 M KOH.

2.6. Electrochemical measurement

The tests are performed on a CHI760E electrochemical workstation. The as-prepared samples are used as the working electrode. The counter electrode is graphite rod. The reference electrode is saturated calomel electrode (SCE), and the electrolyte is 1.0 M KOH. The potentials are calibrated against reversible hydrogen electrode (RHE) through: E_{RHE} = E_{SCE} + 0.241 + 0.059 × pH. The liner scanning voltage (LSV) test is performed at scan rate of 10 mV s⁻¹ with iR-correction. Electrochemical impedance spectroscopy (EIS) is carried out with a frequency range from 0.1 to 10⁵ Hz. The electrochemical active surface area (ECSA) of the samples is estimated by: ECSA = C_{dl}/C_s, where C_{dl} is double layered capacitance calculated through the cyclic voltammetry (CV) tested in a non-Faradaic region with the scan rates of 50, 60, 70, 80, 90 and 100 mV s⁻¹, respectively; C_s is the specific capacitance of the 1.0 M KOH, which is 40 μF cm⁻² [25]. Turnover frequency (TOF) is calculated

according to previous reports [26].

2.7. AEM water electrolyzer assembly and measurement

The AEM water electrolyzer comprise of the anode (Fe-NiS₂/NCNT, 2.25 cm²), cathode (1 mg/cm² of commercial Pt/C on carbon cloth, 2.25 cm²), anion exchange membrane (AEM, FAA-3-PK-130), and gas diffusion layer (nickel foam NF). The electrolyte is 1 M KOH, which is supplied to the AEM electrolyzer at a flow rate of 100 mL/min at 50 °C. Durability performance of the AEM electrolyzer is tested at a constant potential for 200 h.

3. Results and discussion

3.1. Theoretical prediction of OH⁻ enrichment effect

In alkaline electrolyte, OH⁻ ions are the reactant of OER reaction and its attraction on the catalyst surface is the first reaction step [27]. Hence, one can expect that the reaction rate of OER would be promoted by the increased local OH⁻ concentration around the catalyst surface. Accordingly, DFT calculations and finite-element numerical method are conducted to evaluate the OH⁻ enrichment effect of NCNT. The OH adsorption energy (E_{ads}) on the electropositive site of nitrogen-doped carbon (-1.48 eV) is higher than graphite carbon site (-1.22 eV), see Fig. 1 and S1. This indicates that the introduction of nitrogen-doping offers chemical active site facilitating the local attraction of OH⁻. In addition, in order to quantitatively estimate the impact of NCNT introduction on the enhancement of surface OH⁻, the Gouy-Chapman-Stern model is used to map the OH⁻ concentration in the Helmholtz layer of NCNT electrode (Fig. 1). It can be seen that, a constant anode potential of 1.5 V vs. RHE would lead to a nine times increase in the local OH⁻ concentration near the polarized NCNT surface than that in bulk solution. These results successfully predict the accumulation of OH⁻ near the NCNT surface, and thus verifying the feasibility of introducing NCNT in the OH⁻ enhancement OER catalyst design. That is, when NCNT is implemented near the active Fe-NiS₂ surface, the OER catalytic performance would be significantly promoted by the increased concentration of local OH⁻ reactant.

3.2. Composition and morphology

In view of the theoretical guidance, the Fe-NiS₂/NCNT catalyst is fabricated (Fig. 1). Briefly, the NCNT is grown on carbon cloth substrate by a thermal chemical vapor deposition process using DMF as carbon

source. Then, the NiFe LDH nanosheets are grown on the NCNT through hydrothermal reaction, and Fe-NiS₂ is obtained after sulfuration treatment. In this design strategy, the NCNT rooted from the carbon cloth fibers would serve as conductive tentacle attracting the OH⁻. This would lead to its local accumulation near the NCNT, and thus synergistically promote the OER performance of adjacent Fe-NiS₂ pre-catalyst. The XRD analysis show that Fe-NiS₂/NCNT consists of NiS₂ crystalline (Fig. 2a). This is very similar with the XRD pattern of Fe-NiS₂ (Fig. S2), indicating that the introduction of NCNT has no effect on the crystal structure. The SEM images of NCNT, NiFe LDH/NCNT and Fe-NiS₂/NCNT are presented in Fig. 2b-c, and S3. One can see that, the diameter of NCNT is about 30 nm, forming a three-dimensional nanostructured conductive matrix (Fig. 2b and S4). After hydrothermal reaction and sulfuration treatment, the surface of NCNT is covered with abundant Fe-NiS₂ nanosheets, showing a rough surface morphology (Fig. 2c). In Table S1, the SEM-based energy dispersive spectroscopy (SEM-EDS) analysis of Fe-NiS₂/NCNT indicates that the atomic composition of N is 2.65%. In the TEM image of Fe-NiS₂/NCNT, it can be clearly seen that NCNT is in close contact with Fe-NiS₂ nanosheets (Fig. 2d,e). That is, the NCNT would also act as conductive bridge in between carbon cloth and Fe-NiS₂ catalyst. The high-resolution TEM (HRTEM) image further displays a lattice space of 0.28 nm corresponding to the NiS₂ (200) plane, further confirming the formation of NiS₂ crystalline in Fe-NiS₂/NCNT (Fig. 2f). Also, the element mapping of Fe-NiS₂/NCNT also confirms the abundant N-doping in the NCNT matrix (Fig. 2g). Moreover, the surface area and pore size distribution of NCNT and Fe-NiS₂/NCNT are evaluated by N₂ adsorption/desorption isotherms (Fig. S5a). NCNT and Fe-NiS₂/NCNT present type-IV isotherms with an H₃ hysteresis loop desorption, implying the existence of mesopores structure, which are also verified by the pore size distribution curve (Fig. S5b). The mesoporous channels provide abundant active sites that is a key prerequisite to achieve high OER activity. The BET surface area of Fe-NiS₂/NCNT is calculated to be 19.60 m² g⁻¹, which is smaller than that of NCNT (33.33 m² g⁻¹), indicating the nanosheets are successfully covered onto NCNT.

3.3. Experimental analysis of OH⁻ enrichment effect

In order to demonstrate the effect of OH⁻ concentration on the overall OER kinetics, the KOH concentration-dependent OER Tafel slope profiles is measured (Fig. 3a). It is found that, as the KOH concentration increases, the Tafel slope of both Fe-NiS₂ and Fe-NiS₂/NCNT decreases. This suggests that the increased OH⁻ concentration plays important role in promoting the OER reaction kinetics. Moreover, under the same KOH concentration, the Tafel slope of Fe-NiS₂/NCNT is always smaller than

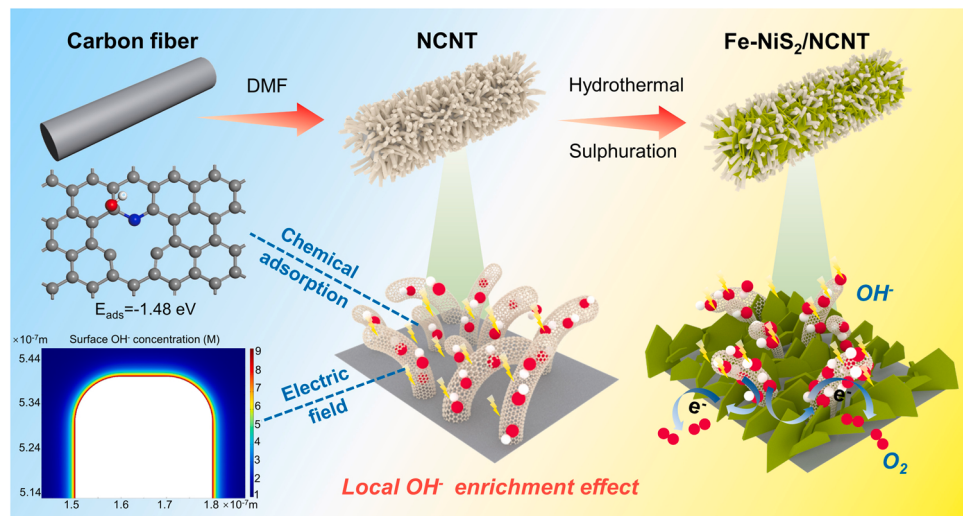


Fig. 1. Schematic of the OH⁻ ions local enhancement strategy in the development of Fe-NiS₂/NCNT OER catalyst.

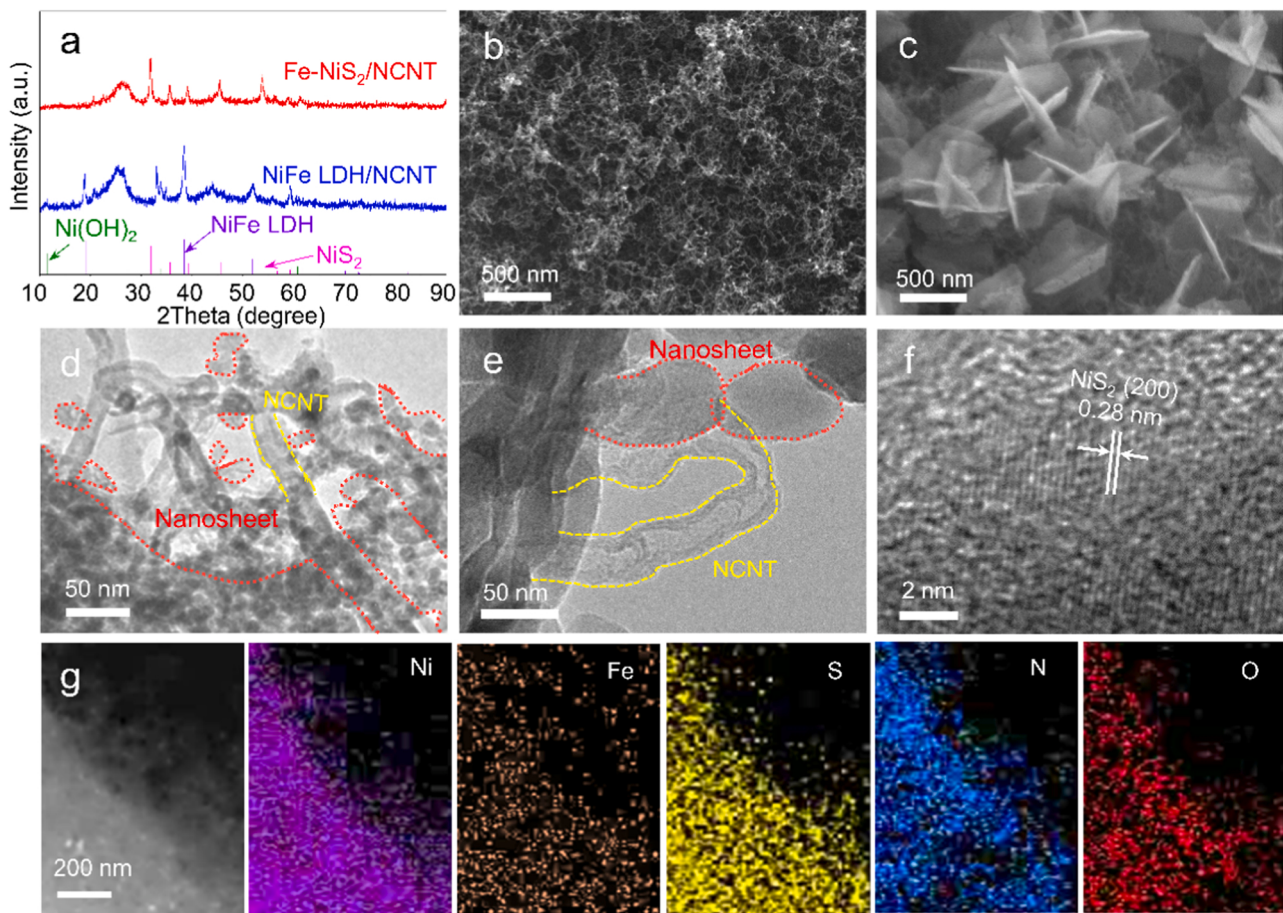


Fig. 2. (a) XRD patterns of Fe-NiS₂/NCNT and NiFe LDH/NCNT; SEM images of (b) NCNT and (c) Fe-NiS₂/NCNT; (d-e) TEM images of Fe-NiS₂/NCNT; (f) HRTEM image and (g) element mapping of Fe-NiS₂/NCNT.

that of Fe-NiS₂, particularly at low concentration range, evidencing the OH⁻ enrichment effect induced by NCNT.

The Zeta potential reflects the charges on the electrode surface, and therefore would provide additional information on the interaction between NCNT and OH⁻. As shown in Fig. 3b, Fe-NiS₂/NCNT exhibits a more negative zeta potential (-25.8 mV) in 1 M KOH than Fe-NiS₂ (-19.8 mV). This suggests more OH⁻ ions are accumulated in the inner Helmholtz layer of Fe-NiS₂/NCNT, which provides further evidence for the local OH⁻ enrichment effect due to the presence of NCNT [28]. In addition, in-situ Raman spectroscopy analysis is also employed to clarify the OH⁻ capturing behavior of NCNT. Fig. S6 shows the time-dependence of the O-H stretching Raman band of NCNT and bare carbon cloth samples measured at 1.3 V vs. RHE. The broad band in the 3800–3000 cm⁻¹ region is attributed to the O-H stretching in OH⁻ [29]. One can see that, during the test, the O-H stretching Raman band in the contour plot of NCNT changes from yellow to red due to its increased signal intensity (Fig. 3c). In contrast, the contour plot of bare carbon cloth shows that the OH⁻ stretching intensity band remains intact in the continuous test (Fig. 3d). This observation provides additional experimental support on the accumulated OH⁻ ions around the NCNT surface.

3.4. Catalytic OER performance

Fig. 4a compares the LSV curves of the as-prepared catalysts toward OER reaction. Obviously, Fe-NiS₂/NCNT exhibits significantly enhanced OER performance than that of Fe-NiS₂ and NCNT. Specifically, Fe-NiS₂/NCNT displays excellent OER catalytic activity with low overpotentials of 247 and 281 mV to reach the current densities of 100 and 200 mA cm⁻², respectively, superior to that of Fe-NiS₂ (330 and

392 mV), NCNT (512 and 593 mV) and Ir/C (450 and 620 mV), see Fig. 4b. These results highlight that the OH-enriched effect of NCNT and the synergistic effect of Fe-NiS₂ and NCNT are critical for promoting the OER performance of Fe-NiS₂. Additionally, the Tafel slope of Fe-NiS₂/NCNT (49 mV dec⁻¹) in Fig. 4c is smaller than Fe-NiS₂ (87 mV dec⁻¹), NCNT (154 mV dec⁻¹) and Ir/C (94 mV dec⁻¹), further confirming that the introduction of NCNT enhances the OER reaction kinetics. The excellent alkaline OER catalytic activity of Fe-NiS₂/NCNT exceeds most of the recently reported OER catalysts, see Fig. 4d and Table S2 [6, 30–38]. Noted that, Fe-NiS₂/NCNT also shows improved OER performance over NiFe LDH/NCNT, implying the higher intrinsic activity of sulfide in catalyzing OER reaction (Fig. S7). Moreover, the HER performance of Fe-NiS₂/NCNT electrocatalyst is also evaluated. Fig. S8 shows that Fe-NiS₂/NCNT exhibits favorable HER activity and presents lower overpotentials of 77 and 196 mV at 10 and 100 mA cm⁻², respectively.

In order to exclude the effect of geometric surface area on the catalytic performance, the ECSA of these catalysts are estimated (Fig. S9). As shown in Fig. 4e, the C_{dl} of Fe-NiS₂/NCNT, Fe-NiS₂ and NCNT electrodes are 59.1, 47.5 and 24.6 mF cm⁻², respectively. The corresponding ECSA for Fe-NiS₂/NCNT is 1477.5 cm², which is higher than those on Fe-NiS₂ (1187.5 cm²) and NCNT (615.0 cm²). This demonstrates that, the introduction of NCNT also leads to an exposure of more accessible active surface of Fe-NiS₂. Therefore, to clarify the inherent catalytic activity of these catalysts, their ESCA normalized LSV curves (*j*_{ECSA}) are presented. The results show that Fe-NiS₂/NCNT has much higher intrinsic OER activity than Fe-NiS₂ and NCNT (Fig. S10). For example, Fig. 4f shows that, at an operation potential of 1.53 V vs RHE, the *j*_{ECSA} value of Fe-NiS₂/NCNT (0.259 mA cm⁻²) is much higher than those of Fe-NiS₂

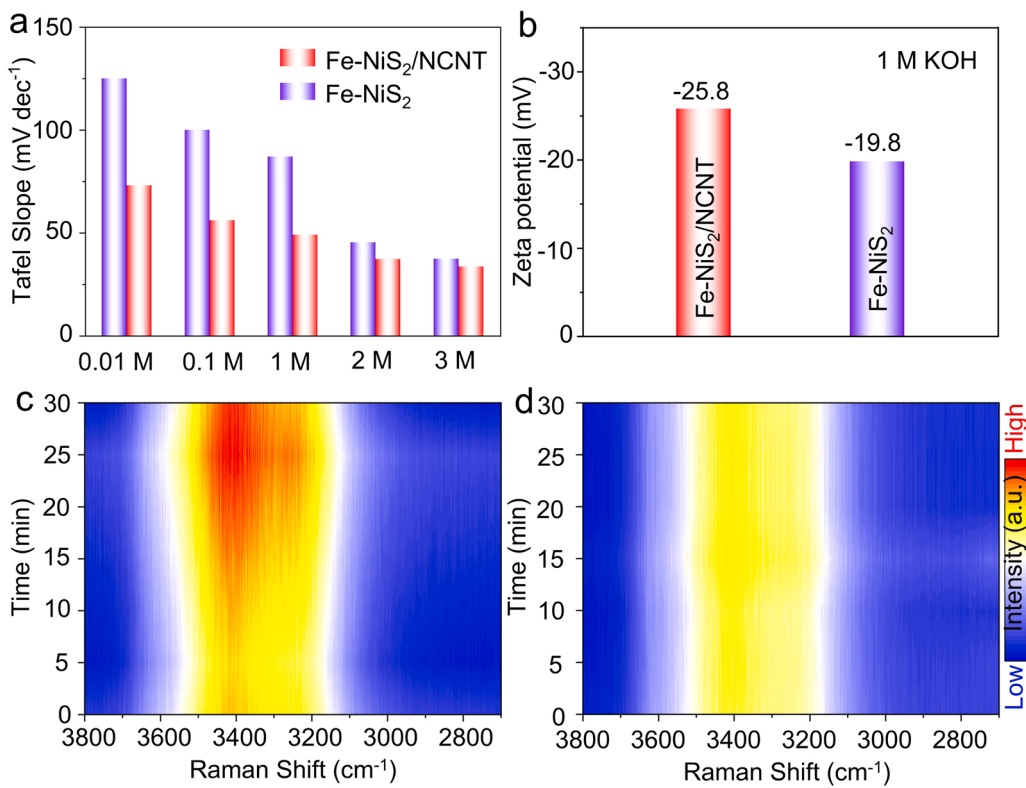


Fig. 3. (a) KOH concentration-dependent OER Tafel slope profiles for Fe-NiS₂ and Fe-NiS₂/NCNT; (b) Zeta potential of Fe-NiS₂ and Fe-NiS₂/NCNT in 1 M KOH; contour plots of the in-situ Raman spectra of (c) NCNT and (d) bare carbon cloth samples measured at 1.3 V vs. RHE.

(0.057 mA cm⁻²) and NCNT (0.015 mA cm⁻²). In addition, the TOF analysis shows that the Fe-NiS₂/NCNT exhibits a much higher TOF of 0.252 s⁻¹ at an overpotential of 300 mV for OER compared with Fe-NiS₂ (0.036 s⁻¹) and NCNT (0.011 s⁻¹), as shown in Fig. 4f and Fig. S11. These results provide further evidence for the improved catalytic performance of Fe-NiS₂/NCNT by the introduction of NCNT.

To evaluate the charge transfer properties of the catalytic OER reaction, EIS analysis is also performed. The Nyquist plots show that the charge-transfer resistance (R_{ct}) of Fe-NiS₂/NCNT (8.4 Ω) is lower than Fe-NiS₂ (12.0 Ω), see Fig. S12. This suggests that, in Fe-NiS₂/NCNT, the existence of NCNT allows rapid migration of electrons from carbon substrate to the Fe-NiS₂ surface, accelerating its charge transportation dynamics. Temperature dependent EIS spectra are also performed at 298–328 K, as shown in Fig. 4g and S13. As expected, the R_{ct} of all catalyst samples decreases with the increase of temperature. At each temperature, the electronic resistance of Fe-NiS₂/NCNT is the lowest, further confirming the fast electron transfer rate promoted by NCNT. Furthermore, the reaction kinetics of OER on different electrocatalyst surfaces is estimated by the apparent activation energy (E_a) [39]. The Arrhenius plots of Fe-NiS₂/NCNT, Fe-NiS₂ and NCNT can be found in Fig. 4h and S14. The apparent activation energy for Fe-NiS₂/NCNT and Fe-NiS₂ towards OER reaction is found to be 21.8 and 26.5 kJ mol⁻¹. This result implies that presence of NCNT promotes the OER reaction kinetics contributed by its OH⁻ concentration enhancement effect. Furthermore, the good durability performance of Fe-NiS₂/NCNT under OER reaction is demonstrated by a 100 h continuous test at the current density of 100 mA cm⁻² (Fig. 4i). The excellent structural stability has been verified by the SEM image of Fe-NiS₂/NCNT electrode after extended OER stability tests, in which the architecture is well preserved (Fig. S15). In addition, the Faradaic efficiency (FE) of OER on Fe-NiS₂/NCNT is close to 100%, indicating its high energy conversion efficiency in catalyzing OER reaction (Fig. S16).

3.5. Catalyst surface state in OER reaction

The catalyst usually undergoes oxidation under the high operation potential of OER, and the in-situ converted species is usually considered as the real catalytic phase. Thus, the dynamic change of catalyst surface state during OER reaction is investigated. Fig. 5a-b present the CV curves of Fe-NiS₂ and Fe-NiS₂/NCNT measured in the potential range from 1.07 to 1.67 V vs. RHE and at different scan rates. The cathodic and anodic peaks at 1.40–1.65 V and 1.10–1.30 V vs. RHE represent the pseudo-capacitive behavior of the catalysts, which is typically contributed by a reversible transformation between Ni²⁺ and Ni³⁺ (Ni²⁺↔Ni³⁺) [36]. Obviously, the current density and area of the CV loop for Fe-NiS₂/NCNT is higher than that Fe-NiS₂ and NCNT, which might be contributed by its increased reactive surface. To quantify the redox Ni²⁺↔Ni³⁺ reaction, the surface coverage of Ni²⁺/Ni³⁺ redox pairs (Γ^*) participating in the OER reaction at Fe-NiS₂/NCNT and Fe-NiS₂ electrode are estimated using the following equation [40,41]:

$$I_p = \left(\frac{n^2 F^2}{4RT} \right) \nu A \Gamma^*$$

where I_p is the cathodic/anodic peak current (mA), n is the number of transferred electrons, F is the Faraday's constant (96485 C mol⁻¹), R is the ideal gas constant (8.314 J K⁻¹ mol⁻¹), T is the temperature (298 K), ν is the potential scan rate (mV s⁻¹), and A is the geometric surface area (cm²). Fig. 5c shows that the Γ^* value of Fe-NiS₂/NCNT (1.3×10^{-6} mol cm⁻²) is higher than that of Fe-NiS₂ (1.1×10^{-6} mol cm⁻²). This indicates that, attributed to the OH⁻ enrichment effect of NCNT, there is a higher coverage of electroactive species in Fe-NiS₂/NCNT and thus promoting its OER activity.

Moreover, the in-situ Raman spectra of Fe-NiS₂/NCNT and NiS₂/NCNT are also acquired to monitor their dynamic changes. It can be seen that, from the open-circuit voltage (OCV) to 1.5 V vs. RHE, the peak of Ni-S bond at 477 cm⁻¹ is detected for Fe-NiS₂ (Fig. S17) [42]. As the

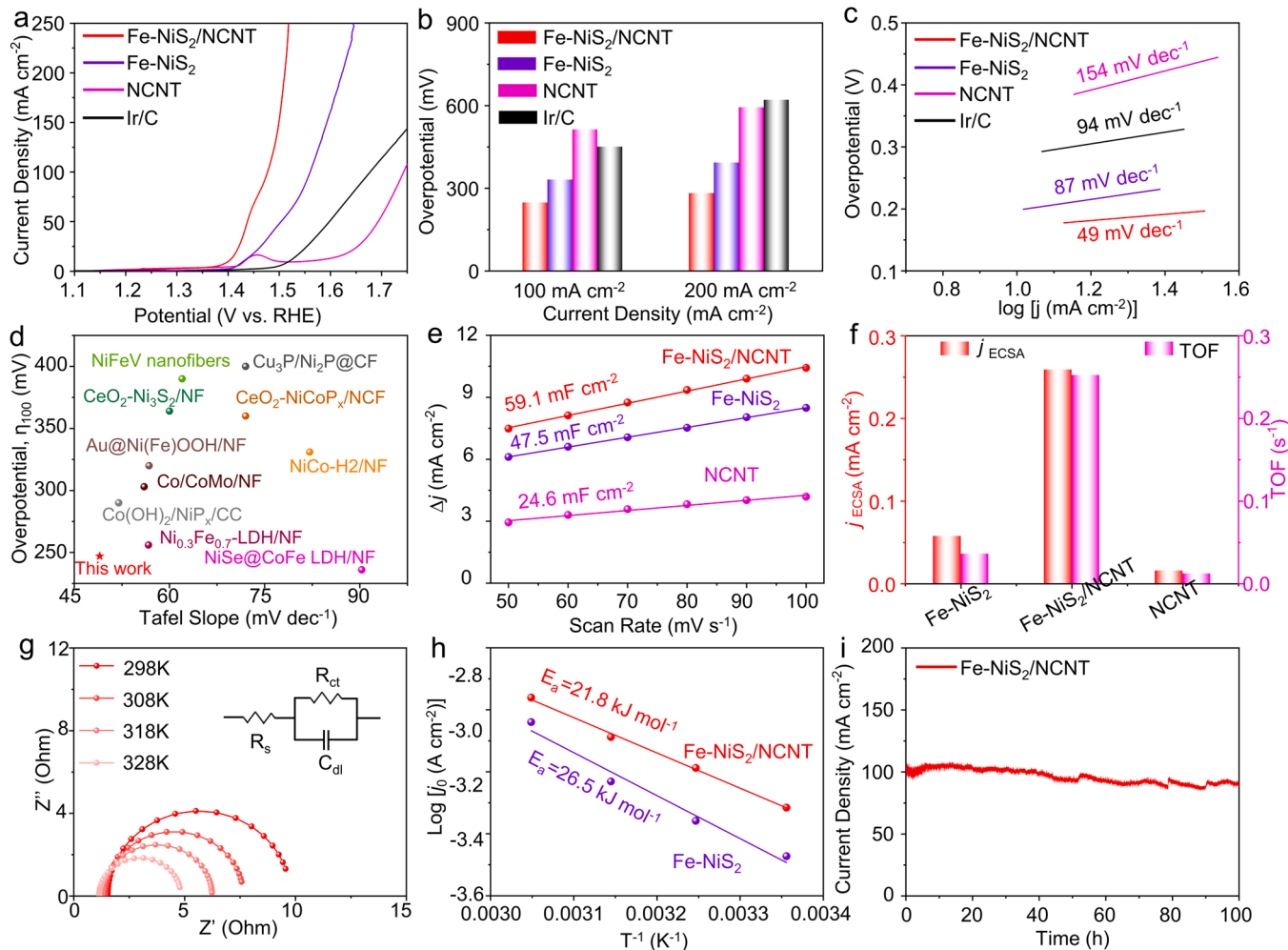


Fig. 4. (a) LSV curves of Fe-NiS₂/NCNT, Fe-NiS₂, NCNT and Ir/C; (b) overpotential of Fe-NiS₂/NCNT, Fe-NiS₂, NCNT and Ir/C; (c) Tafel plots; (d) a comparison of Tafel slope and overpotential with recently reported catalysts [6,30–38]; (e) C_{dl} of catalysts derived from current density versus the scan rate; (f) j_{ECSA} (left) and TOF (right) at 1.53 V vs. RHE; (g) EIS of temperature dependences of charge transfer behavior R_{ct} for Fe-NiS₂/NCNT; (h) Arrhenius plots of j_0 for Fe-NiS₂/NCNT and Fe-NiS₂; (i) stability test of Fe-NiS₂/NCNT at 1.48 V vs. RHE for 100 h in 1.0 M KOH.

potential increased to 1.6 V vs. RHE, the Ni-S bond is vanished and the two new peaks at 474 and 552 cm⁻¹ appears, indicating the formation of γ -NiOOH (Fig. 5d). For comparison, in Fe-NiS₂/NCNT, the peak of γ -NiOOH became visible at a relatively low potential of 1.4 V vs. RHE (Fig. 5e). This indicates that NCNT decoration effectively boosted the in-situ oxidation of Fe-NiS₂ into NiOOH at low working potentials. In other words, these results demonstrate that the OH⁻ enrichment effect of NCNT in Fe-NiS₂/NCNT promotes the transition of Fe-NiS₂ into NiOOH, which is beneficial for OER reaction. In addition, the XPS results demonstrated the presence of Ni, Fe, S, O, N and C elements on the Fe-NiS₂/NCNT surface (Table S3). Specifically, the high resolution XPS spectrum of Ni 2p in Fig. 5f exhibits two main peaks, Ni 2p_{1/2} and Ni 2p_{3/2}, and the characteristic peak at 854.1 eV of Fe-NiS₂/NCNT belongs to Ni²⁺ state of nickel sulfide, whereas Ni³⁺ state can also be detected at binding energy of 857.0 eV [43]. After OER stability test, the Ni²⁺ in Fe-NiS₂/NCNT disappears and the peaks shift towards higher binding energy forming a new peak at 855.9 eV, which can be attributed the existence of nickel oxyhydroxide (NiOOH) species on the catalyst surface [33,44]. These phenomena indicate that the surface of Fe-NiS₂/NCNT has been covered by the evolved oxyhydroxide species, which is regarded as a realistic active component for OER reaction [45]. In Fig. 5g, the Fe 2p spectra of Fe-NiS₂/NCNT shows a same characteristic peak of Fe³⁺ (712.6 eV) before and after OER reaction, indicating the Fe³⁺ state is very stable [46]. The high-resolution O 1 s spectrum for

Fe-NiS₂/NCNT is divided into absorbed H₂O (533.3 eV) and metal hydroxide bond (M-OH; 532.1 eV), see Fig. S18 [47]. After OER reaction, an additional peak belonging to the metal-oxygen bond (M-O; 530.7 eV) is formed, and the intensity of the peak of M-OH (531.5 eV) is enhanced, supporting the formation of NiOOH species [48]. As for S 2p spectrum of Fe-NiS₂/NCNT in Fig. 5h, the peak at 169.2 eV can be assigned to SO₄²⁻ bond due to the surface oxidation, and the other two peaks at 162.7 eV and 163.9 eV corresponds to Ni/Fe-S in Fe-NiS₂/NCNT [49]. After OER reaction, the Ni/Fe-S peak intensity significantly decreases for both catalysts, suggesting that partial sulfur oxidation or dissolution into electrolyte occurs. The above analysis suggests that Fe and S remain in the catalyst after OER reaction. The variation of surface composition before and after OER reaction is shown in Table S3. In Fe-NiS₂/NCNT, Fe dissolution is significantly suppressed with a minor Fe/Ni atomic ratio drop (from 0.49 to 0.40) (Fig. S19). However, this is accompanied by a significant loss of S content. This suggests that Fe is more stable than S in sulfide. This phenomenon is consistent with previous report [9]. Furthermore, it has been demonstrated that Fe-doping enhances the electrical conductivity and alters the binding energy of oxygen intermediates on Ni sites, which benefits the OER activity [50,51]. Therefore, it is concluded that the actual active species of Fe-NiS₂/NCNT pre-catalyst is S, Fe-doped S, Fe-NiOOH rather than NiOOH (Fig. 5i). In addition, the N 1 s spectra of Fe-NiS₂/NCNT can be deconvoluted into three peaks positioned at 398.4 eV, 400.0 eV, and 401.3 eV (Fig. S20),

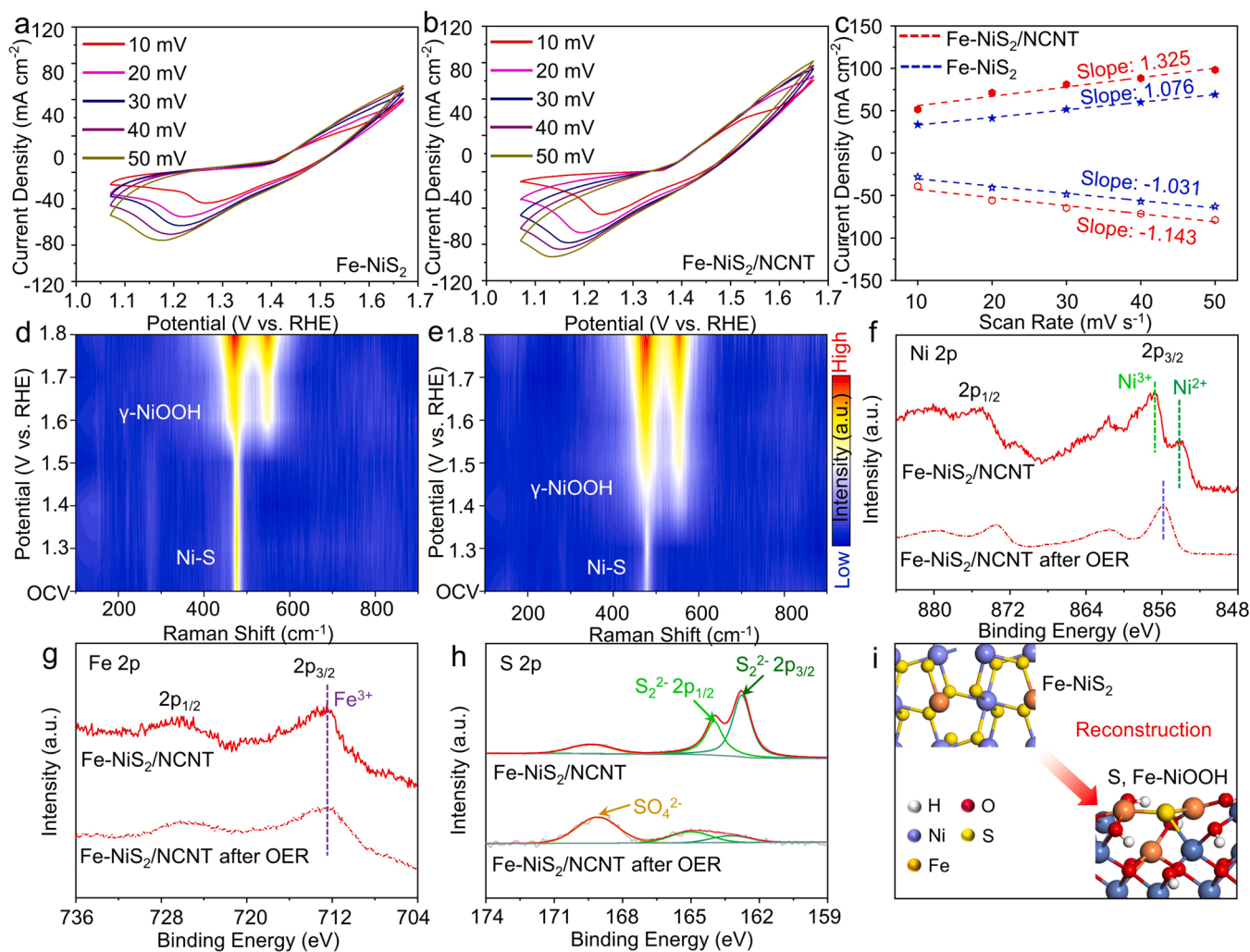


Fig. 5. CV curves of (a) Fe-NiS₂ and (b) Fe-NiS₂/NCNT in 1.0 M KOH at different sweep rates: 10, 20, 30, 40, 50 mV s⁻¹; (c) linear fitting of the anodic and cathodic peak current densities to scan rates; contour plots of the in-situ Raman spectra of (d) Fe-NiS₂ and (e) Fe-NiS₂/NCNT at different potentials; XPS spectra of (f) Ni 2p, (g) Fe 2p and (h) S 2p for Fe-NiS₂/NCNT before and after OER test; (i) illustration of Fe-NiS₂/NCNT reconstruction during OER reaction.

corresponding to pyridinic N, pyrrolic N and graphitic N [52]. Clearly, pyridinic N is the main nitrogen species. It has been suggested that pyridinic N can promote the adsorption and activation of O-containing intermediates, which has a significant impact on the catalytic activity toward OER [53].

3.6. DFT study on OER catalytic origin

The above results clearly demonstrate that the Fe-NiS₂/NCNT pre-catalyst undergoes oxidation and reconstructed into S, Fe-NiOOH, thus governing its intrinsic OER activity. In addition, the in-situ Raman results show that the real catalytic activity is NiOOH, which indicates that the active site is Ni site rather than Fe site. The XPS analysis shows that the valence state of Ni changes after the OER reaction for the Fe-NiS₂/NCNT catalyst, whereas the valence state of Fe remains the same. This also suggests that Ni site is the active site, which is consistent with previous reports [54]. Consequently, DFT calculations with Ni sites as active sites are performed to understand the catalytic origin of S, Fe-NiOOH species. In addition, Fe-NiOOH and NiOOH models are also constructed as the control samples to study the effect of S and Fe doping on OER activity. Noted that, applying a positive potential can only further reduce the OER energy barrier estimated from the analogous chemical reactions in DFT [55,56]. That is, the energy barriers obtained from DFT for analogous chemical reactions serve as the initial or

reference energy barriers, and can be utilized to assess the OER intrinsic activity. Therefore, to simplify the calculation, the DFT analysis is performed based on the NiOOH, Fe-NiOOH and S, Fe-NiOOH models without applying working potential. The Gibbs free energy analysis is employed to further discuss the detailed OER mechanism. The rate determining step (RDS) of OER for NiOOH, Fe-NiOOH and S, Fe-NiOOH is the conversion from [•]OH to [•]O (Fig. S21). The S, Fe-NiOOH exhibits a lower barrier energy (1.53 eV) compared to those of Fe-NiOOH (1.72 eV) and NiOOH (1.89 eV). The calculations reveal that S and Fe co-doping tunes the Gibbs free energy of the formed intermediates and thus exhibit improved OER catalytic activity. Furthermore, Fig. 6a presents the electron localization function (ELF) of Ni-O bond in NiOOH (0.52), Fe-NiOOH (0.68) and S, Fe-NiOOH (0.80). The high ELF of Ni-O bond leads to more positive charge on surface Ni atoms. This high ELF in S, Fe-NiOOH would improve its interaction with OER intermediates, and thus lead to enhanced OER performance [57]. In the density of state (DOS) analysis, S, Fe-NiOOH is found exhibit narrowed bandgap compared with that of NiOOH and Fe-NiOOH, suggesting that S, Fe co-doping can modify the electronic structure of NiOOH and improves the charge transportation performance, facilitating the OER reaction (Fig. 6b).

It is known that, in alkaline electrolyte, OER follows a four electron reaction mechanism:[27]

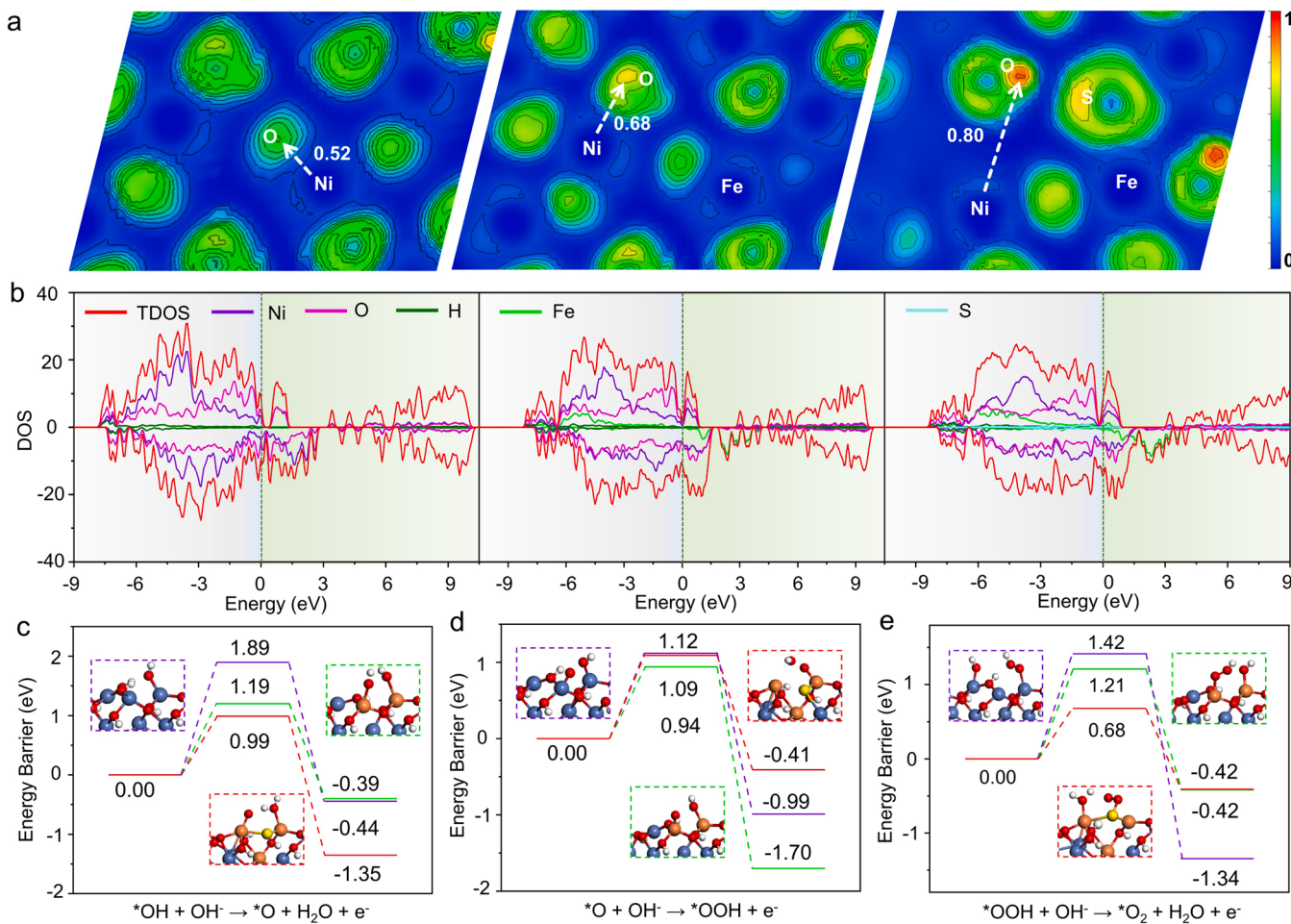


Fig. 6. (a) ELF and (b) DOS analysis of NiOOH, Fe-NiOOH and S, Fe-NiOOH; the energy barrier and corresponding models for (c) $^*\text{OH} + \text{OH}^- \rightarrow ^*\text{O} + \text{H}_2\text{O} + \text{e}^-$, (d) $^*\text{O} + \text{OH}^- \rightarrow ^*\text{OOH} + \text{e}^-$ and (e) $^*\text{OOH} + \text{OH}^- \rightarrow ^*\text{O}_2 + \text{H}_2\text{O} + \text{e}^-$ of NiOOH (blue line), Fe-NiOOH (green line) and S, Fe-NiOOH (red line), the blue, orange, yellow, red and white balls refer to Ni, Fe, S, O and H atom.



The adsorption of OH^- represents the first step of OER reaction. Fig. S22 shows that OH^- adsorption energy on S, Fe-NiOOH (-3.80 eV) and Fe-NiOOH (-3.82 eV) is higher than NiOOH (-3.19 eV), suggesting the incorporation of Fe and S is beneficial for initiating OER reaction. For the step (2), during the transition of $^*\text{OH}$ into $^*\text{O}$, the H atom in OH moves toward adjacent OH species. The energy barrier (E_{barrier}) of this process on NiOOH, Fe-NiOOH and S, Fe-NiOOH is found to be 1.89, 1.19 and 0.99 eV, respectively (Fig. 6c). The lower E_{barrier} on S, Fe-NiOOH implies the transition of $^*\text{OH}$ into $^*\text{O}$ is kinetically favorable in the presence of Fe and S doping. The $^*\text{O}$ to $^*\text{OOH}$ transition step (3) exhibits similar energetics on S, Fe-NiOOH (1.09 eV), Fe-NiOOH (0.94) and NiOOH (1.12 eV), see Fig. 6d. Interestingly, the reaction kinetics of sequential $^*\text{OOH}$ to $^*\text{O}_2$ step is significantly promoted on S, Fe-NiOOH (0.68 eV) over Fe-NiOOH (1.21 eV) and NiOOH (1.42 eV), see Fig. 6e. The final OER step, release of O_2 , is more favorable on NiOOH (-0.94 eV) and S, Fe-NiOOH (-1.04 eV) with lower adsorption energy than Fe-NiOOH (-2.29 eV), see Fig. S23. These results suggest that S, Fe co-decorated NiOOH is more favorable to accelerate OER reaction kinetics.

3.7. AEM water electrolyzer performance

To demonstrate its potential application in water splitting reaction, an AEM electrolyzer is constructed using the Fe-NiS₂/NCNT anode and with a Pt/C coated carbon cloth cathode (Fig. 7a). The polarization curves of AEM electrolyzer systems in 1 M KOH solution are presented in Fig. 7b and Fig. S24. One can see that, the Fe-NiS₂/NCNT||Pt/C-based electrolyzer requires 1.70 V cell potential to deliver an overall water splitting current density of 500 mA cm^{-2} , outperforms that using Fe-NiS₂/NCNT||Fe-NiS₂/NCNT or Ir/C||Pt/C. More importantly, the Fe-NiS₂/NCNT||Pt/C electrolyzer also shows excellent long-term stability in continuous 200 h test at 500 mA cm^{-2} high current density (Fig. 7c). Also, as shown in Fig. 7d, Fe-NiS₂/NCNT demonstrates excellent hydrophilicity in the wettability test. This super-hydrophilic feature would promote the contact of electrolyte with the catalyst surface, and thus facilitate the bubbles release benefiting OER reaction as well [58].

4. Conclusion

In the present study, an enhanced local OH^- reactant concentration design strategy is proposed towards the development of high-performance OER electrocatalysts. This catalyst design strategy is successfully demonstrated by the fabrication of Fe-NiS₂/NCNT catalyst, in which NCNT is introduced within the adjacent Fe-NiS₂ pre-catalyst to form a conductive OH^- reactant attractor network. At the same time, the electropositive sites of NCNT can also effectively adsorb OH^- and

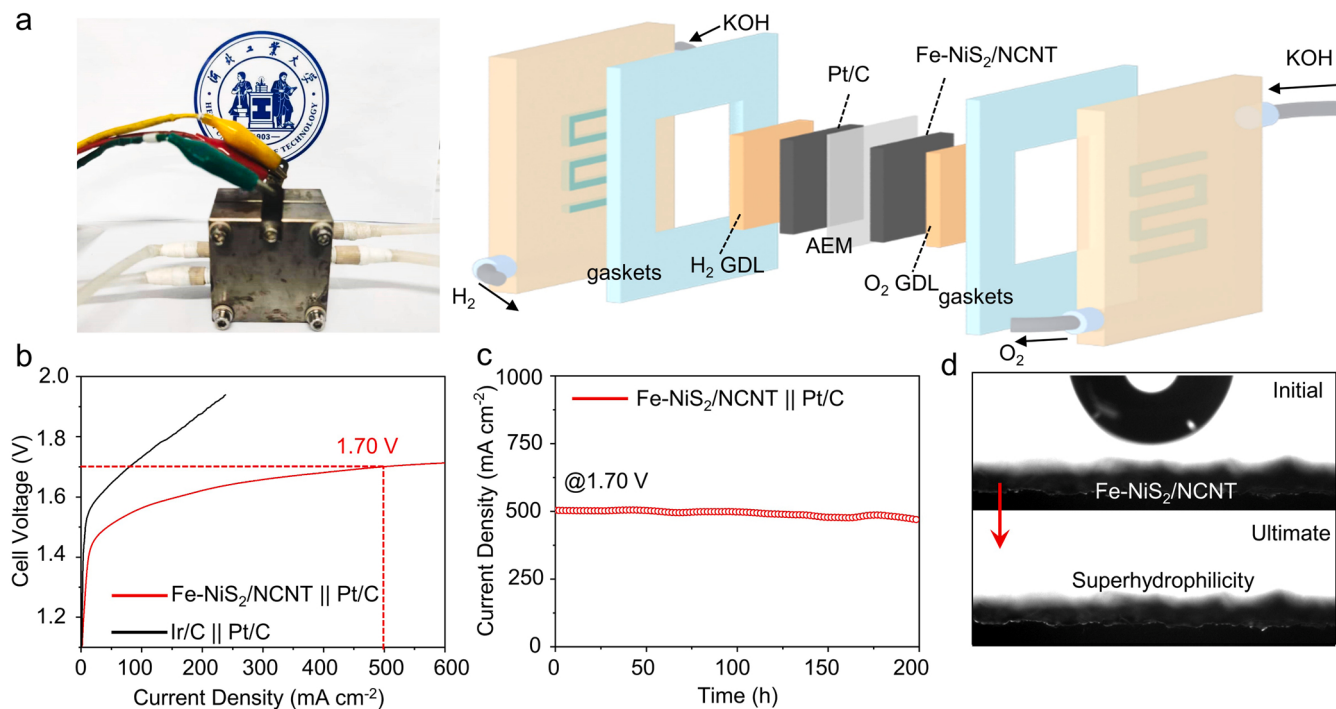


Fig. 7. (a) Schematic for an AEM water electrolyzer based on Fe-NiS₂/NCNT and Pt/C electrode; (b) polarization curves of AEM electrolyzer for Fe-NiS₂/NCNT||Pt/C and Ir/C||Pt/C; (c) time-dependent current density curves of Fe-NiS₂/NCNT||Pt/C for 200 h tested at 1.70 V; (d) wettability test of Fe-NiS₂/NCNT electrode.

increase the OH⁻ concentration around the Fe-NiS₂ surface. Accordingly, the OER performance is promoted by the synergistic effect of the NCNT network with the adjacent Fe-NiS₂ pre-catalyst. Benefited from the enhanced local reaction concentration design, the Fe-NiS₂/NCNT electrocatalyst only requires an ultralow overpotential of 247 mV at 100 mA cm⁻² in 1.0 M KOH. Also, the AEM electrolyzer delivers a cell current density of 500 mA cm⁻² at an only 1.70 V_{cell} with promising long-term durability performance. In addition, experimental analysis clearly demonstrates that the local concentration enrichment of OH⁻ would also accelerate the Fe-NiS₂ reconstitution into S and Fe co-doped NiOOH, which serves as the real OER active species. This study highlights the importance of tailoring the local reactant concentration to design high-performance electrocatalysts.

CRediT authorship contribution statement

Xiaojing Liu: Investigation, Data curation, Formal analysis, Writing – original draft. **Ximeng Zhao:** Investigation, Data curation, Formal analysis. **Shuyi Cao:** Investigation, Methodology. **Mingyi Xu:** Formal analysis. **Yanji Wang:** Project administration. **Wei Xue:** Conceptualization, Project administration, Writing – review & editing. **Jingde Li:** Conceptualization, Writing – review & editing, Supervision, Funding acquisition.

Declaration of Competing Interest

The authors declare that they have no known competing financial interests or personal relationships that could have appeared to influence the work reported in this paper.

Data Availability

Data will be made available on request.

Acknowledgments

This work was supported by the Natural Science Foundation of Hebei Province (B2020202009) and National Natural Science Foundation of China (22278109).

Appendix A. Supporting information

Supplementary data associated with this article can be found in the online version at [doi:10.1016/j.apcatb.2023.122715](https://doi.org/10.1016/j.apcatb.2023.122715).

References

- [1] X. Xie, L. Du, L. Yan, S. Park, Y. Qiu, J. Sokolowski, W. Wang, Y. Shao, Oxygen evolution reaction in alkaline environment: material challenges and solutions, *Adv. Funct. Mater.* 32 (2022) 2110036.
- [2] H. Qian, J. Wei, C. Yu, F. Tang, W. Jiang, D. Xia, L. Gan, In situ quantification of the active sites, turnover frequency, and stability of Ni-Fe (oxy)hydroxides for the oxygen evolution reaction, *ACS Catal.* 12 (2022) 14280–14289.
- [3] S. Lee, I. Kim, H. Cho, C. Kim, Y. Lee, Resolving potential-dependent degradation of electrodeposited Ni(OH)₂ catalysts in alkaline oxygen evolution reaction (OER): In situ XANES studies, *Appl. Catal. B Environ.* 284 (2021), 119729.
- [4] X. Zheng, Y. Cao, Z. Wu, W. Ding, T. Xue, J. Wang, Z. Chen, X. Han, Y. Deng, W. Hu, Rational design and spontaneous sulfurization of NiCo-(oxy) hydroxysulfides nanosheets with modulated local electronic configuration for enhancing oxygen electrocatalysis, *Adv. Energy Mater.* 12 (2022) 2103275.
- [5] X. Shen, H. Li, Y. Zhang, T. Ma, Q. Li, Q. Jiao, Y. Zhao, H. Li, C. Feng, Construction dual-regulated NiCo₂S₄ @Mo-doped CoFe-LDH for oxygen evolution reaction at large current density, *Appl. Catal. B Environ.* 319 (2022), 121917.
- [6] Y. Zhai, X. Ren, Y. Sun, D. Li, B. Wang, S. Liu, Synergistic effect of multiple vacancies to induce lattice oxygen redox in NiFe-layered double hydroxide OER catalysts, *Appl. Catal. B Environ.* 323 (2023), 122091.
- [7] Q. Niu, M. Yang, D. Luan, N.W. Li, L. Yu, X.W.D. Lou, Construction of Ni-Co hydroxide@Ni-Co layered double hydroxide yolk-shelled microrods for enhanced oxygen evolution, *Angew. Chem. Int. Ed.* 61 (2022), e202213049.
- [8] N. Ran, E. Song, Y. Wang, Y. Zhou, J. Liu, Dynamic coordination transformation of active sites in single-atom MoS₂ catalysts for boosted oxygen evolution catalysis, *Energy Environ. Sci.* 15 (2022) 2071–2083.
- [9] Q. Han, Y. Luo, J. Li, X. Du, S. Sun, Y. Wang, G. Liu, Z. Chen, Efficient NiFe-based oxygen evolution electrocatalysts and origin of their distinct activity, *Appl. Catal. B Environ.* 304 (2022), 120937.
- [10] T. Jing, N. Zhang, C. Zhang, S. Moudikoudis, Z. Sofer, W. Li, P. Li, T. Li, Y. Zuo, D. Rao, Improving C–N–FeO_x oxygen evolution electrocatalysts through hydroxyl-modulated local coordination environment, *ACS Catal.* 12 (2022) 7443–7452.

[11] Y. Chen, Y. Wang, J. Yu, G. Xiong, H. Niu, Y. Li, D. Sun, X. Zhang, H. Liu, W. Zhou, Underfocus laser induced Ni nanoparticles embedded metallic MoN microrods as patterned electrode for efficient overall water splitting, *Adv. Sci.* 9 (2022) 2105869.

[12] A. Meena, P. Thangavel, D.S. Jeong, A.N. Singh, A. Jana, H. Im, D.A. Nguyen, K. S. Kim, Crystalline-amorphous interface of mesoporous Ni_2P @ FePO_xH_y for oxygen evolution at high current density in alkaline-anion-exchange-membrane water-electrolyzer, *Appl. Catal. B-Environ.* 306 (2022), 121127.

[13] S. Li, L. Wang, H. Su, A.N. Hong, Y. Wang, H. Yang, L. Ge, W. Song, J. Liu, T. Ma, X. Bu, P. Feng, Electron redistributed S-doped nickel iron phosphides derived from one-step phosphatization of MOFs for significantly boosting electrochemical water splitting, *Adv. Funct. Mater.* 32 (2022) 2200733.

[14] H. Song, J. Wang, Z. Zhang, X. Shai, Y. Guo, Synergistic balancing hydrogen and hydroxyl adsorption/desorption of nickel sulfide via cation and anion dual-doping for boosting alkaline hydrogen evolution, *Chem. Eng. J.* 420 (2021), 129842.

[15] Z. Zhang, C. Feng, X. Li, C. Liu, D. Wang, R. Si, J. Yang, S. Zhou, J. Zeng, In-situ generated high-valent iron single-atom catalyst for efficient oxygen evolution, *Nano Lett.* 21 (2021) 4795–4801.

[16] L. Wu, L. Yu, Q. Zhu, B. McElhenny, F. Zhang, C. Wu, X. Xing, J. Bao, S. Chen, Z. Ren, Boron-modified cobalt iron layered double hydroxides for high efficiency seawater oxidation, *Nano Energy* 83 (2021), 105838.

[17] L. Zhang, W. Tang, C. Dong, D. Zhou, X. Xing, W. Dong, Y. Ding, G. Wang, M. Wu, Bionic sunflower-like structure of polydopamine-confined NiFe-based quantum dots for electrocatalytic oxygen evolution reaction, *Appl. Catal. B Environ.* 302 (2022), 120833.

[18] P.W. Menezes, S. Yao, R. Beltran-Suito, J.N. Hausmann, P.V. Menezes, M. Driess, Facile access to an active gamma-NiOOH electrocatalyst for durable water oxidation derived from an intermetallic nickel germanide precursor, *Angew. Chem. Int. Ed.* 60 (2021) 4640–4647.

[19] H. Lei, L. Ma, Q. Wan, S. Tan, B. Yang, Z. Wang, W. Mai, H.J. Fan, Promoting surface reconstruction of NiFe layered double hydroxide for enhanced oxygen evolution, *Adv. Energy Mater.* (2022) 2202522.

[20] P. Yang, X. Zhang, F. Gao, Y. Zheng, Z. Niu, X. Yu, R. Liu, Z. Wu, S. Qin, L. Chi, Y. Duan, T. Ma, X. Zheng, J. Zhu, H. Wang, M. Gao, S. Yu, Protecting copper oxidation state via intermediate confinement for selective CO_2 electroreduction to C_2 -fuels, *J. Am. Chem. Soc.* 142 (2020) 6400–6408.

[21] F. Gao, S. Hu, X. Zhang, Y. Zheng, H. Wang, Z. Niu, P. Yang, R. Bao, T. Ma, Z. Dang, Y. Guan, X. Zheng, X. Zheng, J. Zhu, M. Gao, S. Yu, High-curvature transition-metal chalcogenide nanostructures with a pronounced proximity effect enable fast and selective CO_2 electroreduction, *Angew. Chem. Int. Ed.* 59 (2020) 8706–8712.

[22] H. Tan, B. Tang, Y. Lu, Q. Ji, L. Lv, H. Duan, N. Li, Y. Wang, S. Feng, Z. Li, C. Wang, F. Hu, Z. Sun, W. Yan, Engineering a local acid-like environment in alkaline medium for efficient hydrogen evolution reaction, *Nat. Commun.* 13 (2022) 2024.

[23] M. Liu, Y. Pang, B. Zhang, P. De Luna, O. Vozny, J. Xu, X. Zheng, C.T. Dinh, F. Fan, C. Cao, F.P. de Arquer, T.S. Safaei, A. Mepham, A. Klinkova, E. Kumacheva, T. Filletier, D. Sinton, S.O. Kelley, E.H. Sargent, Enhanced electrocatalytic CO_2 reduction via field-induced reagent concentration, *Nature* 537 (2016) 382–386.

[24] J.D. Wang, W.R. Hume, Diffusion of hydrogen ion and hydroxyl ion from various sources through dentine, *Int. Endod. J.* 21 (1988) 17–26.

[25] L. Tan, J. Yu, C. Wang, H. Wang, X. Liu, H. Gao, L. Xin, D. Liu, W. Hou, T. Zhan, Partial sulfidation strategy to NiFe-LDH@FeNi₂S₄ heterostructure enable high-performance water/seawater oxidation, *Adv. Funct. Mater.* 32 (2022) 2200951.

[26] L. Yang, L. Huang, Y. Yao, L. Jiao, In-situ construction of lattice-matching NiP₂/NiSe₂ heterointerfaces with electron redistribution for boosting overall water splitting, *Appl. Catal. B Environ.* 282 (2021), 119584.

[27] J. Mohammed-Ibrahim, A review on NiFe-based electrocatalysts for efficient alkaline oxygen evolution reaction, *J. Power Sources* 448 (2020), 227375.

[28] B. Mao, P. Sun, Y. Jiang, T. Meng, D. Guo, J. Qin, M. Cao, Identifying the transfer kinetics of adsorbed hydroxyl as a descriptor of alkaline hydrogen evolution reaction, *Angew. Chem. Int. Ed.* 59 (2020) 15232–15237.

[29] T. Sugimura, S. Kajimoto, T. Nakabayashi, Label-free imaging of intracellular temperature by using the O-H stretching Raman band of water, *Angew. Chem. Int. Ed.* 59 (2020) 7755–7760.

[30] F. Nie, Z. Li, X. Dai, X. Yin, Y. Gan, Z. Yang, B. Wu, Z. Ren, Y. Cao, W. Song, Interfacial electronic modulation on heterostructured NiSe@CoFe LDH nanoarrays for enhancing oxygen evolution reaction and water splitting by facilitating the deprotonation of OH to O₂, *Chem. Eng. J.* 431 (2022), 134080.

[31] M. Chen, H. Li, C. Wu, Y. Liang, J. Qi, J. Li, E. Shangguan, W. Zhang, R. Cao, Interfacial engineering of heterostructured Co(OH)₂/NiP_x nanosheets for enhanced oxygen evolution reaction, *Adv. Funct. Mater.* 32 (2022) 2206407.

[32] H. Ma, Z. Chen, Z. Wang, C.V. Singh, Q. Jiang, Interface engineering of Co/CoMoN/NF heterostructures for high-performance electrochemical overall water splitting, *Adv. Sci.* 9 (2022) 2105313.

[33] X. Liu, S. Jing, C. Ban, K. Wang, Y. Feng, C. Wang, J. Ding, B. Zhang, K. Zhou, L. Gan, X. Zhou, Dynamic active sites in NiFe oxyhydroxide upon Au nanoparticles decoration for highly efficient electrochemical water oxidation, *Nano Energy* 98 (2022), 107328.

[34] M. Chen, D. Liu, J. Feng, P. Zhou, L. Qiao, W. Feng, Y. Chen, K. Wei, In-situ generation of Ni-CoOOH through deep reconstruction for durable alkaline water electrolysis, *Chem. Eng.* 443 (2022), 136432.

[35] S. Wen, J. Huang, T. Li, W. Chen, G. Chen, Q. Zhang, X. Zhang, Q. Qian, K. Ostrivov, Multiphase nanosheet-nanowire cerium oxide and nickel-cobalt phosphide for highly-efficient electrocatalytic overall water splitting, *Appl. Catal. B Environ.* 316 (2022), 121678.

[36] Z. Huang, X. Liao, W. Zhang, J. Hu, Q.J.A.C. Gao, Ceria-promoted reconstruction of Ni-based electrocatalysts toward efficient oxygen evolution, *ACS Catal.* 12 (2022) 13951–13960.

[37] B. Zhang, Z. Wu, W. Shao, Y. Gao, W. Wang, T. Ma, L. Ma, S. Li, C. Cheng, C. Zhao, Interfacial atom-substitution engineered transition-metal hydroxide nanofibers with high-valence Fe for efficient electrochemical water oxidation, *Angew. Chem. Int. Ed.* 61 (2022), e202115331.

[38] H. Liu, J. Gao, X. Xu, Q. Jia, L. Yang, S. Wang, Oriented construction Cu₃P and Ni₂P heterojunction to boost overall water splitting, *Chem. Eng. J.* 448 (2022), 137706.

[39] C. Lv, X. Wang, L. Gao, A. Wang, S. Wang, R. Wang, X. Ning, Y. Li, D. W. Boukhvalov, Z. Huang, C. Zhang, Triple functions of Ni(OH)₂ on the surface of WN nanowires remarkably promoting electrocatalytic activity in full water splitting, *ACS Catal.* 10 (2020) 13323–13333.

[40] A.A. Dubale, Y. Zheng, H. Wang, R. Hubner, Y. Li, J. Yang, J. Zhang, N.K. Sethi, L. He, Z. Zheng, W. Liu, High-performance bismuth-doped nickel aerogel electrocatalyst for the methanol oxidation reaction, *Angew. Chem. Int. Ed.* 59 (2020) 13891–13899.

[41] J. Li, Z. Luo, Y. Zuo, J. Liu, T. Zhang, P. Tang, J. Arbiol, J. Llorca, A. Cabot, NiSn bimetallic nanoparticles as stable electrocatalysts for methanol oxidation reaction, *Appl. Catal. B Environ.* 234 (2018) 10–18.

[42] K. Han, J. Meng, X. Hong, X. Wang, L. Mai, Three-dimensional graphene-supported nickel disulfide nanoparticles promise stable and fast potassium storage, *Nanoscale* 12 (2020) 8255–8261.

[43] S. Lu, X. Shang, L. Zhang, B. Dong, W.-K. Gao, F. Dai, B. Liu, Y. Chai, C. Liu, Heterostructured binary Ni-W sulfides nanosheets as pH-universal electrocatalyst for hydrogen evolution, *Appl. Surf. Sci.* 445 (2018) 445–453.

[44] H. Zhang, X. Li, A. Hähnel, V. Naumann, C. Lin, S. Azimi, S.L. Schweizer, A. W. Maijenburg, R.B. Wehrspohn, Bifunctional heterostructure assembly of NiFe LDH nanosheets on NiCoP nanowires for highly efficient and stable overall water splitting, *Adv. Funct. Mater.* 28 (2018) 1706847.

[45] J. Chen, H. Chen, T. Yu, R. Li, Y. Wang, Z. Shao, S. Song, Recent advances in the understanding of the surface reconstruction of oxygen evolution electrocatalysts and materials development, *Electrochem. Energy Rev.* 4 (2021) 566–600.

[46] T. Gao, Z. Jin, Y. Zhang, G. Tan, H. Yuan, D. Xiao, Coupling cobalt-iron bimetallic nitrides and N-doped multi-walled carbon nanotubes as high-performance bifunctional catalysts for oxygen evolution and reduction reaction, *Electrochim. Acta* 258 (2017) 51–60.

[47] N. Cheng, Q. Liu, A.M. Asiri, W. Xing, X. Sun, A. Fe-doped, Ni₃S₂ particle film as a high-efficiency robust oxygen evolution electrode with very high current density, *J. Mater. Chem. A* 3 (2015) 23207–23212.

[48] H. Wang, C. Li, J. An, Y. Zhuang, S. Tao, Surface reconstruction of NiCoP for enhanced biomass upgrading, *J. Mater. Chem. A* 9 (2021) 18421–18430.

[49] T.X. Nguyen, Y.H. Su, C.C. Lin, J.M. Ting, Self-reconstruction of sulfate-containing high entropy sulfide for exceptionally high-performance oxygen evolution reaction electrocatalyst, *Adv. Funct. Mater.* 31 (2021) 2106229.

[50] J. Zhang, L. Yu, Y. Chen, X.F. Lu, S. Gao, X.W.D. Lou, Designed formation of double-shelled Ni-Fe layered-double-hydroxide nanocages for efficient oxygen evolution reaction, *Adv. Mater.* 32 (2020), e1906432.

[51] W. Liu, X. Hu, H. Li, H. Yu, Pseudocapacitive Ni-Co-Fe hydroxides/N-Doped carbon nanoplates-based electrocatalyst for efficient oxygen evolution, *Small* 14 (2018) 1801878.

[52] T. Jin, X. Liu, Y.-Q. Su, F. Pan, X. Han, H. Zhu, R. Wu, Y. Lyu, Mesoporous carbon-supported ultrasmall metal nanoparticles via a mechanochemical-driven redox reaction: a “Two-in-One” strategy, *Appl. Catal. B Environ.* 294 (2021), 120232.

[53] L. Pei, J. zhong, T. Li, W. Bai, S. Wu, Y. Yuan, Y. Chen, Z. Yu, S. Yan, Z. Zou, CoS₂@N-doped carbon core-shell nanorod array grown on Ni foam for enhanced electrocatalytic water oxidation, *J. Mater. Chem. A* 8 (2020) 6795–6803.

[54] M. Han, N. Wang, B. Zhang, Y. Xia, J. Li, J. Han, K. Yao, C. Gao, C. He, Y. Liu, Z. Wang, A. Seifitkaldani, X. Sun, H. Liang, High-valent nickel promoted by atomically embedded copper for efficient water oxidation, *ACS Catal.* 10 (2020) 9725–9734.

[55] J. Li, G. Liu, J. Fu, G. Jiang, D. Luo, F.M. Hassan, J. Zhang, Y.-P. Deng, P. Xu, L. Ricardez-Sandoval, Z. Chen, Surface decorated cobalt sulfide as efficient catalyst for oxygen evolution reaction and its intrinsic activity, *J. Catal.* 367 (2018) 43–52.

[56] Z. Zhang, C. Feng, D. Wang, S. Zhou, R. Wang, S. Hu, H. Li, M. Zuo, Y. Kong, J. Bao, J. Zeng, Selectively anchoring single atoms on specific sites of supports for improved oxygen evolution, *Nat. Commun.* 13 (2022) 2473.

[57] H. Yang, L. Gong, H. Wang, C. Dong, J. Wang, K. Qi, H. Liu, X. Guo, B.Y. Xia, Preparation of nickel-iron hydroxides by microorganism corrosion for efficient oxygen evolution, *Nat. Commun.* 11 (2020) 5075.

[58] W. Liu, X. Wang, J. Qu, X. Liu, Z. Zhang, Y. Guo, H. Yin, D. Wang, Tuning Ni dopant concentration to enable co-deposited superhydrophilic self-standing Mo₂C electrode for high-efficient hydrogen evolution reaction, *Appl. Catal. B Environ.* 307 (2022), 121201.